Sequestration of orthophosphate by Ca2Al-NO3 layered double hydroxide – Insight into reactivity and mechanism

Belayneh Bekele, Laura Lundehøj, Nicholai Daugaard Jensen, Ulla Gro Nielsen, Claude Forano

Sequestration of orthophosphate by $Ca_2Al\text{-}NO_3$ Layered Double Hydroxide – Insight into reactivity and mechanism.

Belayneh Bekele[a], Laura Lundehøj[b], Nicholai Daugaard Jensen[b,c], Ulla Gro Nielsen[b], Claude Forano[*a]

[a] *Université Clermont Auvergne, CNRS, SIGMA Clermont, ICCF, F-63000 Clermont-Ferrand, France.*

[b] *Department of Physics, Chemistry and Pharmacy, University of Southern Denmark, Campusvej 55, 5230 Odense M, Denmark.*

[c] *ICGM, UMR 5253, CNRS-UM-ENSCM, Place E. Bataillon, CC1701, 34095 Montpellier cedex 05, France.*

Abstract

This study reports the mechanism of reactivity of phosphate anions (HPO_4^{2-}) with $Ca_2Al\text{-}NO_3$ LDH. Sequestration of PO4 by $Ca_2Al\text{-}NO_3$ was quantified by fitting the adsorption isotherm with a Langmuir model. Adsorption capacity (65.2 $mgP.g^{-1}$ of LDH) is greater than the theoretical anion exchange capacity indicating further mechanism of sequestration. Partial dissolution of $CaAl\text{-}NO_3$ results in precipitation of multiple Ca-PO4 phases. Combined characterizations by XRD, ^{27}Al and ^{31}P NMR, FTIR/Raman and SEM highlight the competitive precipitation of hydroxyapatite and brushite within the LDH structure. Multiple environment of PO4 anions offer promising perspective for $CaAl\text{-}NO_3$/PO4 as slow release fertilizer.

Keywords: Layered Double Hydroxides; $Ca_2Al\text{-}NO_3$ hydrocalumite, orthophosphate; adsorption, hydroxyapatite, brushite.

1. Introduction

Inorganic orthophosphate (PO4) is an essential resource for agriculture and animal feed additives. Indeed, 82% and 7% of their production are used respectively as fertilizers and food production (Schroeder et al., 2009). Unfortunately, PO4 is a non-renewable resource and the impoverishment of world stocks threaten the food supply to the world population (EU Report, 2013). With a mean production of 160 Mt per year over 16 000 Mt estimated reserves, in 100 years PO4 scarcity will be a severe problem. Added to these human and economic dangers, a major environmental concern arises from the dissemination of PO4 in the environment and its accumulation in surface waters through land farming and waters discarded from wastewater treatment plants (WWTP) causing harmful eutrophication of inland and coastal waters (Oliveira et al., 2013; Farley et al, 2012). Consequently, the development of sustainable PO4 management processes is of high societal concern.

Recovery of PO4 from WWTP and processing as recycled PO4 slow release fertilizers (SRF), are under intensive investigations to both limit phosphate wastes and improve circular economic model of this critical raw material (Cieslik et al., 2017; Desmidt et al., 2015). Most sustainable water-cleaning processes in WWTPs target the precipitation of phosphate as struvite ($NH_4MgPO_4.6H_2O$) (Ye et al., 2014) or hydroxyapatite ($Ca_5(PO_4)_3(OH)$, HAP) (Chen et al., 2009), for subsequent reuse as fertilizers. However struvite production is limited to large scale WWTPs and has so far failed to reach a sustainable economic model (Talboys et al., 2016).

Moreover, the low solubility of struvite and hydroxyapatite in water (Ricardo et al., 2012) limit their use as efficient SRF. Selective adsorption of PO4 from wastewaters by inorganic adsorbents that can be recycle once loaded with PO4 as SRF appears as an alternative green technology.

Layered double hydroxides (LDH) are natural and synthetic inorganic solids with a layered structure and general chemical formula $[M^{2+}_{1-x}M^{3+}_{x}(OH)_2]^{x+}[A^{n-}_{x/n}.mH_2O]^{x-}$ (M^{2+}, M^{3+} and A^{n-} being divalent and trivalent metals and anionic species). They display unique anion exchange properties largely investigated for the removal of oxoanions (NO_3^-, PO_4^{3-}, CrO_4^{2-}, AsO_4^{3-},…) (Lazaridis et al., 2003) as well as they rank amongst the most selective and efficient adsorbents for PO4 anions (Xu et al., 2010; Zhou et al., 2011; Bernardo et al., 2017; Everaert et al., 2018). Among the LDH, hydrocalumite-like LDH, a Ca_2Al-LDH display a very high chemical reactivity with PO4 leading to great quantity of PO4 removed from water, i.e. as high as 400 mg PO4 per gram of LDH exceeding the theoretical anion exchange capacities (Zhou et al., 2011). This behavior makes Ca_2Al- LDH a very promising PO4 sorbents and potential SRF. Few studies have investigated PO4 release from Ca_2Al-PO4 phases prepared by PO4 loading on Ca_2Al LDH and their use as slow-release fertilizers. Interestingly, PO4-loaded hydrocalumite has demonstrated synergistic performances for plant growth and development of bacteria (*Bradyrhizobium elkanii*) responsible for N_2 fixation (Jia et al., 2016).

The mechanism of adsorption of phosphate by Ca-based LDH adsorbents is still under examination (Radha et al., 2005). Some authors claimed that PO4 adsorption follows a topotactic anion exchange reaction with intercalation of HPO_4^{2-} anions in between the LDH layers (Radha et al., 2005). However, most convincing results clearly show that Ca_2Al LDH undergo a progressive dissolution followed by the immediate precipitation of various Ca-PO4 phases (Lu et al., 2016; Zhou et al., 2012). The dissolution/precipitation phenomenon is driven by the

difference between the solubility's of CaAl-LDH and most of the common calcium phosphate phases (Table 1). Hydroxyapatite ($Ca_5(PO)_4(OH)$) and brushite ($CaHPO_4.2H_2O$) (often referred to DCPD for dicalcium phosphate dihydrate) are the most commonly reported calcium phosphate phases that can form from a reaction between Ca_2Al-LDH and PO4 (Khitous et al., 2016; Vieille et al., 2003). Brushite was obtained when PO4 adsorption was performed at acidic pH (pH 5) while in basic medium (pH 11) HAP predominantly precipitates (Tsuji et al., 2014). Jeong-Woo Son et al. (Jeong-Woo Son et al., 2015) confirmed these results for phosphate removal by hydrocalumite at basic pH but they observed the precipitation of other phases (gibbsite, boehmite, calcite). The total conversion of hydrocalumite into one of these phases should result in more than 388 mg of adsorbed PO4 (or 127 mg P) per g of hydrocalumite, values much higher than reported in literature (Lu et al., 2016). The structure and composition of the precipitated Ca-PO4 phase as well as the rate of Ca_2Al-LDH conversion are strongly dependent on various parameters such as $Ca^{2+}/PO4^{3-}$ molar ratio, pH, PO4 concentration. Moreover, the mechanisms of PO4 adsorption and phase conversion are mostly ignored.

Conversion into hydroxyapatite is a limiting factor for a 100% PO4 recovery and may hinder applications of these materials as SRF because extreme pH conditions would be needed to desorb PO4 from HAP (Vieille et al., 2003).

As Ca_2Al LDH have a great ability for PO4 sequestration and potential release, there is a need for further investigations in order to better understand the mechanism involved in this reaction and the role of chemical composition and morphology to control PO4 adsorption and release. Therefore, our study focused on Ca_2Al-NO_3 LDH phase whose reactivity toward PO4 adsorption has not been yet investigated. Combination of XRD, solid state NMR spectroscopy,

and electron microscopy characterization was implemented to identify the CaPO4 phases formed and to assess the mechanism of reactivity of phosphate anions with $Ca_2Al\text{-}NO_3$ LDH materials.

2. Materials and methods

2.1. Materials

All the reagents were analytical grade and used without further purification. $Ca(NO_3)_2{\cdot}4H_2O$, $Al(NO_3)_3{\cdot}9H_2O$, NaOH, K_2HPO4, (L)-ascorbic acid, hexaammonium heptamolybdate $(NH_4)_6Mo_7O_{24}.4H_2O$), sulfuric acid (H_2SO_4), potassium antimony(III) oxide tartrate $(K(SbO)C_4H_4O_6.0.5H_2O)$ were purchased from Sigma-Aldrich. Adsorption studies were performed using K_2HPO_4. Deionized water was used exclusively in all procedures.

2.2. Synthesis of $Ca_2Al\text{-}NO_3$

$Ca_2Al\text{-}NO_3$ was synthesized by the co-precipitation method in a reactor using peristaltic pumps for simultaneous addition of Ca^{2+}/Al^{3+} metal salts and NaOH in order to keep the pH constant following the procedure published by Vieille et al. (Vieille et al., 2003). The Ca^{2+}/Al^{3+} molar ratio was fixed to 2 and the reagent concentrations equal to 1M and 2M respectively for ($[Ca^{2+}] + [Al^{3+}]$) and NaOH. The synthesis was performed at a pH = 11.5 and under N_2 flow to prevent CO_3^{2-} contamination. The reaction was vigorously stirred and completed in 4-5 h. The resulting slurry was aged at room temperature for 24 h. The mixture was centrifuged and the solid washed thoroughly with deionized water and dried at 40 °C for 24h.

2.3. Adsorption isotherms and modeling

The adsorption isotherm experiments were carried out in 2-ml Eppendorf vials. 15 mg of $Ca_2Al\text{-}NO_3$ LDH was suspended in 1.5 ml of K_2HPO_4 aqueous solution with concentrations ranging from 10 to 1000 mg $P.L^{-1}$ (0, 50, 100, 200, 300, 400, 500, 600, 700, 800, 900, 1000 $mgP.L^{-1}$) (P-refers to phosphorous). Suspensions were shaken for 2h00 at 20°C under air atmosphere in order to achieve the adsorption equilibrium (Khitous et al., 2016). The supernatants were separated using centrifugation (14000 rpm, 21475 G-force, 20 min) and pH values were measured to be in the range of 8.1±0.4 throughout the adsorption experiment. Concentrations of phosphate in the solution was determined using a Nicolet Evolution 500 UV-Vis spectrophotometer at λ = 880 nm, following the Molybdenum blue method (Broberg et al., 1988).

The adsorption capacity of the sorbent was measured by the difference between the initial and remaining concentrations of phosphate. The equilibrium adsorption concentrations, q_e ($mg.g^{-1}$), were calculated according the following equation $q_e = \frac{V(C_0 - C_e)}{W}$, where c_o is the initial concentration of (mg P. L^{-1}); c_e is the equilibrium concentration (mg $P.L^{-1}$); V is the volume of the solution used (L); and W is the weight of the adsorbents (g). Sorption isotherms were obtained by plotting experimental qe versus ce. The adsorption isotherms were analyzed using the linearized equations of Langmuir and Freundlich, sorption models, expressed as:

Langmuir: $\frac{c_e}{q_e} = \frac{1}{q_m K} + \frac{c_e}{q_m}$ (1)

Freundlich: $q_e = K_F c_e^{1/n}$ (2)

where c_e (mg.L^{-1}) is the concentration of phosphate at equilibrium and q_e (mg.g^{-1}) is the sorption capacity of the solid at equilibrium. K (L/mg) is Langmuir constant, q_m (mg.g^{-1}) is the saturated sorption capacity of sorbent. K_F and n are Freundlich parameters. K_{DR} (mol^2/J^2) is the activity coefficient. R is the universal gas constant (8.314 J/mol K), and T (K) is temperature.

2.4. Phosphate Exchange with LDH

The phosphate exchange experiments were carried out in 30 ml adsorption vials with 90 mg of LDH and 9 ml of a K_2HPO_4 aqueous solution at 20°C under air atmosphere. The K_2HPO_4 concentrations equal to 0.3, 0.4, 0.5, 0.6, 0.7, 0.8, and 0.9 g HPO_4^{2-}.L^{-1}. The mixtures were stirred for 5h. Solids were separated by centrifugation (14000 rpm, 21475 G-force, 20 min) and washed, repeatedly. Precipitates were dried at 40 °C for 24h. pH values of supernatants were measured to be in the range of 8.2±0.3 throughout the exchange experiment. The concentration range was selected in order to vary the initial HPO_4^{2-}/Ca_2Al-NO_3 mass ratio from 32.6 to 97.9 mgP.g^{-1} of CaAl-NO_3. Considering that such concentration correspond to mass ratio from the early stage of adsorption to saturation we then prepared a series of PO4 loaded samples representative of all the steps of reaction.

2.5. Characterization techniques

Chemical analyses of the LDH were conducted using the ICP-OES after dissolving the samples in 1 M HNO_3 solution. X-ray diffraction (XRD) measurements were performed on a Philips X'Pert Pro diffractometer using CuKα radiation (λ = 1.5405 Å). PXRD patterns were recorded over the 5–70° 2θ range at an accelerating voltage of 40 kV, a current of 30 mA, a scan speed of 2°min^{-1}. Fourier-transform infrared (FTIR) spectra were recorded with a Nicolet-5700

spectrophotometer in the range of 400–4000 cm^{-1} using the KBr pellet technique. The Raman spectra were recorded from 150 to 1500 cm^{-1} at room temperature using a confocal micro-Raman spectrometer (T64000 Jobin Yvon) with an excitation wavelength of 514.5 nm (argon-ion laser-line). Spectra were acquired at a spectral resolution of 1 cm^{-1} with charge coupled device (CCD) multichannel detector cooled by liquid nitrogen to 140 K coupled with Olympus confocal microscope. SEM images were recorded using a JSM-7500F FESEM operating at 3 KV. Samples to be imaged were mounted on conductive carbon adhesive tabs. ICP-AES analyses were realized with a HORIBA-Jobin-Yvon ULTIMA C spectrometer.

^{27}Al MAS and ^{27}Al 3QMAS NMR spectra were recorded on a Varian INOVA 600 MHz NMR spectrometer (14.1 T) equipped with a 3.2 mm triple resonance MAS probe using 15 kHz spinning speed and a 1s relaxation delay. ^{27}Al MAS NMR spectra were recorded using a short, selective $\pi/18$ pulse to ensure quantitative spectra. Quantitative ^{31}P MAS NMR MAS spectra were recorded on a JEOL 500 MHz NMR spectrometer (11.7 T) using a 3.2 mm double resonance probe, a $\pi/4$ pulse, a spinning speed of 13 kHz, and a relaxation delay (typically 480-540 s) optimized for each sample. 85 % phosphoric acid (0.0 ppm) and 1 M $AlCl_3$ have been used as reference for ^{27}Al and ^{31}P, respectively. Deconvolutions of the ^{27}Al and ^{31}P MAS NMR spectra has been performed using QuadFit (Kemp et al., 2009) and MestReNova.

3. Results and Discussion

3.1. Structure and chemical analysis of Ca_2Al-NO_3

The chemical composition ($Ca_{1.91}Al(OH)_{5.82}(NO_3).1.63H_2O$) of the as-prepared Ca_2Al-NO_3 LDH phase, determined from ICP-AES and TGA data, is in good agreement with the chemical formula expected for a pure synthetic NO_3-hydrocalumite. The high pH value (11.5)

used for the synthesis ensured a total coprecipitation of Ca^{2+}/Al^{3+} metal ions. Indeed, the experimental Ca^{2+}/Al^{3+} ratio (1.91) is close to the ideal composition (Ca^{2+}/Al^{3+} = 2) expected from initial molar ratio used. The powder X-ray diffractogram (PXRD) (Fig. 1A) and the FTIR spectrum (Fig. 1B) of $Ca_2Al\text{-}NO_3$ LDH confirmed the formation of the desired material. Indeed PXRD exhibits the structural features including sharp diffraction lines of a well-crystallized $Ca_2Al\text{-}NO_3$ hydrocalumite phase (Renaudin et al., 1999). The cell parameters were refined in the trigonal space group $P\bar{3}c1$ (Fig. 1). The main structural difference compared to the hydrotalcite structure arises from the distortion of the octahedral layer due to the hepta-coordination of Ca^{2+} ions (6+1) bonded to six OH groups and an intercalated H_2O molecule (Fig. SI-1). This corrugated layered structure is associated to typical Ca,Al–OH, Ca,Al–O and (Ca,Al)–O–(Ca,Al) lattice vibrations located at 782, 592, 527 and 420 cm^{-1}, respectively (Zhang et al., 2011). Intercalation of NO_3^- anions was confirmed by the strong infrared absorption at 1380 cm^{-1} and 854 cm^{-1} relative respectively to the antisymmetric stretching ν_3 and out-of-plane bending ν_2 vibrations of the D_{3h} NO_3^- anions. The broad vibrations between 3400 cm^{-1} and 3650 cm^{-1} are characteristics of all LDH and arises from the symmetric and asymmetric stretching (ν(OH)) of the hydroxide layers and intercalated water molecules (Fig. 1B), 3640 cm^{-1} and 34493 cm^{-1}, respectively for free (Ca_2Al)-O-H groups and H-bonded interlayered water molecules. The bending mode of interlayer water molecules appears between 1622-1637 cm^{-1}. $Ca_2Al\text{-}NO_3$ was precipitated as large hexagonal platelets with sizes between 1-3 μm and thickness ranging between 25-110 nm leading to a high aspect ratio (Fig. 7A) and a low BET specific surface area of 11 $m^2.g^{-1}$. ^{27}Al MAS NMR experiment was employed to assess the purity of the parent $Ca_2Al\text{-}NO_3$ LDH (Fig. SI-2). The spectrum was simulated to determine the purity of the Ca_2Al-LDH. The isotropic chemical shift $\delta_{iso}(^{27}Al)$ = 11.0(4) ppm is in agreement

with the value reported by Qiu et al. (Qiu et al., 2015) and Jensen et al. (Jensen et al., 2016) for Ca_2Al-LDH intercalated respectively with NO_3^- or para-aminosalicylate, respectively. From 90-95 % of the intensity originates from Ca_2Al-LDH, when the contribution from the ^{27}Al satellite transitions (ca 5 %) to the center band is included (Table SI-1 and Fig. SI-2a). We note that a Lorentzian line broadening gave the best fit. Moreover, the spinning sidebands in the ^{27}Al MAS NMR spectrum had a clear indication of dynamics on the time scale of the 1st order quadrupole interaction (MHz) (Fig. SI-2) as earlier reported (Di Bitetto et al., 2017). It slightly differs from the value $\delta_{iso}(^{27}Al)$ = 9.5(4) ppm reported for Ca_2Al-Cl by Andersen et al. (Andersen et al., 2002). This small variation is due to a change of anion, as also seen for MgAl- and ZnAl-LDH (Pushparaj et al, 2015; Sideris et al., 2012; Sideris et al., 2008).

3.2. Adsorption isotherm of PO4 by Ca_2Al-NO_3

In order to monitor the reactivity of Ca_2Al-NO_3 material with phosphate and to quantify the amount of sequestrated PO4, Ca_2Al-NO_3 was suspended at 20°C and for 2h00 with solutions containing increasing amounts of HPO_4^{2-} anions (section 2.2) and the PO4 content adsorbed per gram of sorbent versus PO4 equilibrium concentration (qe vs ce) was plotted (Fig. 2A). The isotherm plot is typical of an H-type adsorption isotherm curve according Giles's classification (Giles et al., 1974). This adsorption behavior clearly indicates a high affinity of PO4 anions toward the Ca_2Al-LDH matrix. Both Langmuir and Freundlich models have been used to fit phosphate adsorption by LDH (Hatami et al., 2018; Wan et al., 2017). The Langmuir model assumes monolayer adsorption on a homogeneous surface with no interactions between the adsorbed molecules; while the Freundlich model is often used to describe chemisorption on heterogeneous surface (Chen et al., 2015). Both models were used to fit our experimental data.

The Langmuir model give the best linear fit (with R^2 >0.9980) adsorption constants were determined from the slope and intercept of the plots (Fig.2B and Table SI-2). The experimental PO4 adsorption capacity of $Ca_2Al\text{-}NO_3$ LDH is equal to 65.20 $mgP.g^{-1}$, a value higher than the one expected for a pure anion exchange reaction of HPO_4^{2-} (52.75 $mgP.g^{-1}$), 1.23 time higher, and much higher if we consider PO_4^{3-} exchange (35.17 $mgP.g^{-1}$, 1.85 time higher). Such a high PO4 adsorption capacity was already reported in the literature (Jia et al., 2016, Lu et al., 2016) for $Ca_2Al\text{-}Cl$ LDH (59.55 $mg.g^{-1}$). Nature of the intercalated anion (NO_3^- vs Cl^-) does not affect the total PO4 sequestration but seems to play a role on the mechanism of interaction (Langmuir vs Freundlich)..

It must be mentioned that in our case PO4 adsorption experiments were performed at kinetic equilibrium and that no Ca^{2+} nor Al^{3+} ions were detected in the supernatants. Indeed Ca^{2+} release percentage compared to total Ca^{2+} amount was negligible, less than 2.82% at 0 mgP/L, and decreased to zero till 0.6 mgP/L (Fig. SI-3). Moreover, the amount of phosphate uptake by the $Ca_2Al\text{-}NO_3$ LDH are much lower than the values expected for a total conversion of $Ca_2Al\text{-}NO_3$ into hydroxyapatite (126.6 mg $P.g^{-1}$) or brushite (211.0 $mgP.g^{-1}$). Dissolution/precipitation is probably not total and the mechanism of transformation of CaAl LDH appears much more complex than described in the literature. Consequently, we performed XRD and ^{27}Al SSNMR on samples loaded with increasing amounts of PO4 in order to follow structural change.

3.3. Dynamic and Reactivity of PO4 anions with $Ca_2Al\text{-}NO_3$ LDH

3.3.1. Ex-situ and in-situ XRD experiments.

Ex-situ PXRD patterns (Fig. 3-A) were recorded for $Ca_2Al\text{-}NO_3$ LDH contacted with HPO_4^{2-} solutions under batch reaction conditions. HPO_4^{2-} anions react with the LDH structure

from a very low PO4 loading (32.6 mg $P.g^{-1}$ LDH; Ca-0.3P). At 43.5 mg $P.g^{-1}$ LDH (Ca0.4P), (002) and (004) the most intense reflections of $Ca_2Al\text{-}NO_3$ pristine material have vanished meanwhile some new diffraction reflections appear that accounts for the formation of new phases. These new phases were identified from comparison of PXRD diffractograms of calcium phosphate phases known to appear during PO4 reaction with hydrocalumite, $Ca_5(PO_4)_3(OH)$ (hydroxyapatite; 09-0432 JCPDS file), $CaHPO_4$ (monetite; monoclinic, 09-0080 JCPDS file), $Ca(HPO_4).2H_2O$ (Brushite; triclinic 09-0077 JCPDS file), octacalcium phosphate ($Ca_8H_2(PO_4)_6.5H_2O$ (OCP) and $Al(OH)_3$ (Gibbsite; 33-0018 JCPDS file). Table SI-3 display the Bragg distances for the reflections of all Ca-xP samples and reference phases (Brushite, hydroxyapatite, gibbsite). A comparison of the PXRD patterns evidence the multiple reactivity of phosphate anions with $Ca_2Al\text{-}NO_3$ giving rise to a competition between exchange reactions into the Ca_2Al structure and precipitation of Ca/PO4 phases.

First, the presence of the characteristic (002)/(110) diffraction doublet from Gibbsite (4.814 Å and 4.390 Å), appear at the lowest PO4 loading (Ca-0.3P), which confirm dissolution of $Ca_2Al\text{-}NO_3$. However, from the point of view of the PXRD data, the amount of Gibbsite does not increase noticeably when increasing phosphate loading, suggesting that dissolution of the pristine layered structure is only partial. This dissolution is confirmed by the occurrence at higher PO4 loading of some reflections from the mineral hydroxyapatite including the (002), (102), and the (121)/(211)/(112)/(300)/(202) reflections at 2θ = 25.90(3), 28.19(3)° and 31–35° 2θ respectively. Reflections assigned to the HAP phase are broad with a low intensity, due to particles with small sizes and low crystallinity. For Ca_2Al-Cl hydrocalumite, PO4 adsorption leads to a collapse of the structure and the formation of hydroxyapatite following a dissolution/precipitation mechanism (Jeong-Woo et al. 2016). Formation of brushite is also suggested by the sharp

reflection at 29.42(3)°, whose intensity increases with PO4 adsorption. This reflection is unambiguously assigned to the (-141) reflection from brushite.

Interestingly, the two intense reflections at 7.564 Å and 3.782 Å with a spacing ratio of 2.0 are observed for all samples. They cannot account for any known calcium phosphate phases but can be explained by a shift of the $Ca_2Al\text{-}NO_3$ (002) and (004) reflection to high 2θ values. Simultaneously intense carbonate vibration bands are present for all phases. This cannot account for the precipitation of calcium carbonate phase such as calcite reported by Jeong-Woo et al. (Jeong-Woo et al., 2016) as corresponding diffraction lines are not observed in the XRD patterns. This CaAl phase with a mean interlayer spacing or basal spacing (d_{bs}) of 7.564 Å must arise from the topotactic transformation of the pristine $Ca_2Al\text{-}NO_3$ LDH (d_{bs} = 8.513 Å) into a $Ca_2Al\text{-}CO_3$ LDH that display a shortest basal spacing (Renaudin et al., 1999; François et al., 1998). Contamination by CO_2 and conversion into CO_3^{2-} is favored by the basicity of the CaAl matrix. This reactivity can be explained by the high stability of the monocarboaluminate phase against both dissolution and phosphate reaction. Obviously phosphate anions cannot be exchanged and stabilized in the Ca_2Al galleries.

In conclusion, the XRD patterns of all samples clearly show a mixture of one or more following phase $Ca_2Al\text{-}NO_3$, $Ca_2Al\text{-}CO_3$, $Al(OH)_3$, $Ca_5(PO_4)_3(OH)$ and $Ca(HPO_4).2H_2O$. These results indicate a different reactivity toward HPO_4^{2-} for $Ca_2Al\text{-}NO_3$ compared to $Ca_2Al\text{-}Cl$. Indeed, Zhou et al. (Zhou et al., 2012) reported that under PO4 adsorption and for a similar range of pH $Ca_2Al\text{-}Cl$ undergoes a complete transformation into a mixture of gibbsite, hydroxyapatite and tricalciumphosphate ($Ca_3(PO_4)_2$). When adsorption is performed at lower pH values using $H_2PO_4^-$ aqueous solution again transformation of $Ca_2Al\text{-}Cl$ is total. However, the resulting calcium phosphate formed deviate between the reported studies. For example, brushite is the

main calcium phosphate phase and gibbsite is converted into $AlPO_4$ for Jia et al. (Jia et al., 2016)) and Lu et al. (Lu et al., 2015) while Quian et al. (Quian et al., 2012) reported the conversion of hydrocalumite into HAP, $CaCO_3$ and $Al(OH)_3$ at pH = 5.0

In-situ PXRD experiments were conducted on the $Ca_2Al\text{-}NO_3$ sample, previously wetted as a paste (solid:water mass ratio = 2:1), loaded in a home-made diffraction cell (Fig. SI-4). The solid was in contact with a 2M HPO_4^{2-} solution (Fig. 3-B) in order to force the exchange by HPO_4^{2-} and minimize the dissolution reaction. Under such conditions of in-situ XRD exchange reaction, the high solid/liquid ratio must limit the dissolution of the NO_3-hydrocalumite and prevent the precipitation of Ca-PO4 phase. The designed cell insures a fast PO4 diffusion to the LDH adsorption sites. A topotactic phase transformation of the pristine material occurs in less than 14 min as shown by the in-situ XRD pattern (Fig. 3-B). A group of three new diffraction lines (10.64(5) Å, 5.28(2) Å, and 3.50(1) Å), with integer spacing ratio (L1/L2 = 2.02; L1/L3 : 3.04), clearly accounts for the formation of a layered phase with a basal spacing mean value of 10.57(5) Å. This 1.957 Å increase of the interlayer distance was also observed when $Ca_2Al\text{-}NO_3$ was contacted with pure water. This structural expansion is reversible under hydration/dehydration process. Thus, this well-defined structural expansion arises from the hydration of the interlayer and the intercalation of a single layer of water molecules but has only previously been observed for $Ca_2Al\text{-}NO_3$ phase. The fast hydration reaction is probably a key step in the dissolution and phosphate reaction of the NO_3-hydrocalumite as H_2O molecules can diffuse easily in the interlayer domains. While NO_3-containing LDH are known to be the most reactive LDH phases towards anion exchange reactions and particularly with orthophosphate anions, condensation of HPO_4^{2-} with the LDH layer occurs prior to exchange preventing the formations of CaAl-PO4 phase.

3.3.2. FTIR and Raman analysis

The strong structural changes undergo by the $Ca_2Al\text{-}NO_3$ phase upon reaction with phosphate, evidenced by XRD analysis, are clearly confirmed by analysis of the Raman (Fig. 4) and FTIR (Fig. SI-5) spectra. First of all, PO4 the vibration bands (Table 2) related to PO4 groups increase during PO4 adsorption as shown on both FTIR and Raman spectra. Loading of $HPO4^{2-}$ leads to the removal of NO_3^- anions which is linked to the decrease of the $\nu_3(NO_3)$ stretching band intensity (1055 cm^{-1}). The formation of $Ca_2Al\text{-}CO_3$ LDH, as suggested by the XRD data (section 3.3.1), is confirmed by the appearance of a broad and intense $\nu_3(CO_3)$ multiplet band (1350-1550 cm^{-1}) (Fig. SI-5). The large feature of the CO_3 vibration bands, unusual for LDH material, must account for the presence of other carbonated phase such as carbonated substituted HAP (Gibson et al., 2002). At low frequencies, the symmetric (ν_2) (433 and 450 cm^{-1}) and asymmetric (ν_4) (582, 593, 609 cm^{-1}) bending modes of the PO_4^{3-} anions (Fig. SI-5) overlap with the lattice vibrations $\nu_{Al(OH)6}$ ofromgibbsite (534 cm^{-1}) and hydrocalumite-like phases (580, 528, 425 cm^{-1}). The splitting of the ν_4 PO4 vibration band into 3 bands accounts for the multiplicity of environment in the HAP, brushite and substituted-CO_3 HAP structure as reported by the literature (Swamiappan et al., 2016). Resolution of several MO-H vibration feature increases from Ca-03P to Ca-09P, due to a clear observation of the νas and νs vibrations of $Al(OH)_3$ Gibbsite (3470, 3527 and 3619 cm^{-1}) superimposed on the HAP bands (3527 and 3619 cm^{-1}, 3100 – 3400 cm^{-1}).

3.3.3 ^{27}Al NMR and ^{31}P MAS NMR characterizations

^{27}Al and ^{31}P SSNMR were used to investigate the structural changes of $Ca_2Al\text{-}NO_3$ during reaction with HPO_4^{2-} and to quantify the relative concentration of the different phosphate phases formed. The ^{27}Al MAS NMR spectra (Fig. 5) all show one resonance in the octahedral range in agreement with the coordination of Al in the LDH structure. In addition, a small amount of tetrahedral Al is seen at $\delta_{iso}(^{27}Al) \approx 73$ ppm, constituting less than 5% in all the ^{27}Al NMR spectra except for the $Ca_2Al\text{-}NO_3$ with 0 and 0.9P loading. Upon phosphate exposure of 0.3P an upfield shoulder to the LDH resonance assigned to AOH appears (Jensen et al., 2016); Pushparaj et al., 2015). Different models for simulation of the 0.3P ^{27}Al MAS NMR spectrum has been applied but an unambiguous model could not be identified. However, it was estimated that 15-30 % of the Al belonged to the LDH. Furthermore, a slight shift in $\delta_{iso}(^{27}Al)$ in the LDH resonance from 11.0(4) to 11.3(4) ppm was observed indicating a change in the intercalated anion, e.g., carbonate as seen by PXRD (Fig. 3-A). At higher phosphate loadings the AOH phase is clearly the dominating phase and consequently the center of the signal is located below 10 ppm. Moreover, the total width of the spinning side band manifold (not shown) changes from ≈400 kHz to ≈600 kHz implying a 50 % increase of the quadrupole interaction of the predominant ^{27}Al resonance. Thus, at high P loading the predominant Al species is AOH, which has a stronger quadrupole interaction (2.5 MHz) than Ca_2Al-LDH (1.6 MHz) (Jensen et al., 2016), c.f., Table SI-2. However, Ca_2Al-LDH might still be present with relative Al concentration up to 10-15 % but not distinguished due to the overlap between the LDH and AOH resonances. Hence, the ^{27}Al MAS NMR confirms dissolution of the LDH and precipitation of aluminum hydroxide (AOH) upon phosphate exposure.

The ^{31}P MAS NMR is a very sensitive probe of the phosphorus speciation and it is therefore possible to distinguish between e.g., different mineral phases.

The ^{31}P MAS NMR spectra for the $Ca_2Al\text{-}NO_3$ all show one resonance at 3 ppm with one set of weak spinning sideband which is indicative of orthophosphate in agreement with earlier studies (Bernardo et al., 2017). The resonance can be adequately fitted with four resonances as seen in the deconvolutions in Fig. 6 and the obtained parameters from deconvolutions are summarized in Table 3. The dominating resonance at $\delta_{iso}(^{31}P)$ = 3.0(3) ppm constitutes 71-79 % of the phosphates species and is based on the isotropic shift assigned to hydroxyapatite ($Ca_{10}(PO4)_6(OH)_2$) (Aue et al., 1984; Rothwell et al., 1980). This is in agreement with the PXRD, where formation of $Ca_5(PO4)_3(OH)$ (HAP) is clearly observed. The small resonance at $\delta_{iso}(^{31}P)$ = 1.4-1.7 ppm is assigned to brushite constituting 6-9% of the sample (Aue et al., 1984; Rothwell et al., 1980). The two resonances at $\delta_{iso}(^{31}P) \approx$ 4.3-4.5 and 5.6-6.0 ppm constitute a total of 16-21 % of the samples. The latter resonance ($\delta_{iso}(^{31}P)$ = 5.6-6.0 ppm) agrees well with a dehydrated oxyhydroxyapatite, $Ca_{10}(PO_4)_6(OH)_{2-2x}O_x$, which may precipitate during phosphate adsorption experiments. Thus, that ^{31}P NMR confirms that the $CaAl\text{-}NO_3$ LDH degrades during the adsorption experiments and mainly hydroxyapatite is formed, which are in agreement with earlier studies for Cl-hydrocalumite (Gibson et al., 2002; Swamiappan et al., 2016: Renaudin et al., 1999).

3.3.4 Morphological evolution under PO4 adsorption

Adsorption of HPO_4^{2-} causes strong changes of the $Ca_2Al\text{-}NO_3$ morphology as shown by SEM analysis (Fig. 7). Indeed, the large hexagonal platelets of the pristine material (Fig.7-A),

with sizes in the range 1-2 μm, undergo a partial dissolution followed by a nucleation/crystallization process occurring at the surface of CaAl-NO_3 particles. Fig.7-B,C and D display these small HAP nanocrystals (size < 100nm) with needle shape homogeneously dispersed all over the solid. Moreover, at 0.6P loading (Fig 7-C) well defined crystals are clearly observed whose parallelepiped forms look like that of the brushite crystals (Onac et al., 2009). It is clear that some of the large hexagonal platelets are still present at high PO4 loading. These observations confirms the hypothesis of formation of Ca_2Al-CO_3, $Ca_5(PO_4)_3(OH,CO_3)$ and $Ca(HPO_4).2H_2O$ (Fig. 7D).

3.4 Mechanism of HPO_4^{2-} reactivity with Ca_2Al-NO_3 LDH

According results from combined PXRD, ^{27}Al and ^{31}P SSNMR, Raman, FTIR and SEM analysis, HPO_4^{2-} anions react spontaneously with Ca_2Al-NO_3 LDH in solution. While PO4 anion exchange was reported into Zn_2Al and Mg_2Al LDH to give respectively Zn_2Al-HPO_4^{2-} (Steftel et al., 2018) and Mg_2Al-HPO_4^{2-} (Everaert et al., 2016), Ca_2Al-HPO_4 LDH was not formed, indicating that if HPO_4^{2-} anions intercalates in between the hydrocalumite layers they react with the layer to destroy the structure. Reaction proceeds according the competing formation of HAP (eq. 1), brushite (eq.2) and Ca_2Al-CO_3 (eq.3):

$Ca_2Al(OH)_6.(NO_3).nH_2O_{(s)} + 6/5HPO_4^{2-}{}_{(aq.)} \Leftrightarrow 2/5Ca_5(PO_4)_3(OH)_{(s)} + Al(OH)_{3(s)} + 7/5OH^-{}_{(aq.)} + NO_3^-{}_{(aq.)} + (n+6/5)\ H_2O$ (eq. 1)

$Ca_2Al(OH)_6.(NO_3).nH_2O_{(s)} + 2HPO_4^{2-}{}_{(aq.)} + 4H_2O \Leftrightarrow 2CaHPO_4.2H_2O_{(s)} + Al(OH)_{3(s)} + 3OH^-{}_{(aq.)} + NO_3^-{}_{(aq.)} + nH_2O$ (eq. 2)

$Ca_2Al(OH)_6.(NO_3).nH_2O_{(s)} + 1/2CO_3^{2-}{}_{(aq.)} \Leftrightarrow Ca_2Al(OH)_6.(CO_3)_{0.5}.nH_2O_{(s)} + NO_3^-{}_{(aq.)}$ (eq. 3)

This result is supported by the adsorption data (section 3.2) that indicates an adsorption capacity greater than expected for a pure anion exchange reaction. However the Langmuir adsorption behavior does not evidence this multiple reactivity because both brushite and HAP formations are strongly thermodynamically favorable.

Unlike most of the data published on hydrocalumite/phosphate reactivity that evidence the conversion of Ca_2Al-Cl into hydroxyapatite, our results show that i) brushite is also formed and ii) part of Ca_2Al LDH remains due to a stabilization by CO_3^{2-} intercalation.

A phosphate concentration of only 400 P $mg.L^{-1}$ is sufficient for the Ca_2Al-NO_3 structure to collapse, i.e. a $HPO4^{2-}/Ca^{2+}$molar ratio of 0.189 while for a total conversion of hydrocalumite into brushite or hydroxyapatitie $HPO4^{2-}/Ca^{2+}$molar ratio of 1.0 and 0.6 are needed. At maximum adsorption, 48.0% of Ca_2Al-NO_3 were converted into calcium phosphate phases, HAP ($Ca_5(PO4)_3(OH)$) and brushite ($Ca(HPO_4).2H_2O$). Obviously, when Ca_2Al-NO_3 is contacted with a solution of HPO_4^{2-} salt, HPO_4^{2-} diffuse easily inside the layered structure up to the Ca^{2+} reactive sites thanks to a fast hydration of the structure (in-situ PXRD) that increases the interlayer distance and opened the structure for PO4 diffusion. The various phosphorus environments shown by ^{31}P NMR indicate that HPO_4^{2-} reaction probably occurs at the Ca_2Al layer surface through an initial complexation of Ca^{2+} ions assisted by both the expulsion of the labile coordinated water and the hydrolysis of Ca-OH bonds. Clearly the corrugated Ca_2Al layers do not stabilize enough the Ca^{2+} ions inside the hepta-coordinated sites. Ca^{2+} ions can easily diffuse out of the layers. Chemical extraction of Ca^{2+} ions and formation of hydrated [Ca-PO4] complexes are the preliminary steps of condensation of Ca-PO4 phases (Fig. 8). Costless energy surface nucleation is then favored. Competition occurs between precipitations of hydroxyapatite and brushite minerals. Even if HAP (PO_4^{3-}/Ca^{2+} =3/5) must be preferentially favored when

surface PO_4^{3-}/Ca^{2+} ratio increases Brushite (PO_4^{3-}/Ca^{2+} =1/1) was also forms as a secondary phase even at such high pH ($\frac{pK2+pK3}{2} = 9.94$). The presence of carbonate in the medium may quenched the formation of calcium phosphate phase, resulting in the stabilization of the CO_3-hydrocalumite like structure (PXRD, FTIR and Raman data). Interestingly, as shown by scanning electron microscopy, brushite and HAP crystallites with a wide distribution of particle size from nanometer to micrometer are dispersed all over the remaining CO_3-hydrocalumite phase. Such composite material with embedded Ca-PO4 phases could give promising result for slow-released phosphate fertilizers. The recycling and reuse of phosphorus could therefore be achieved.

4. Conclusion

This study highlights the specific reactivity of Ca_2Al-NO_3 hydrocalumite-like LDH toward phosphate sequestration. Up to 65.20 $mgP.g^{-1}$ was loaded into the resulting composite, values greater than the anion exchange capacity of Ca_2Al-NO_3. A mixture of brushite, HAP and Ca_2Al-CO_3 LDH phases was obtained allowing a distribution of PO4 structures and morphologies. As HAP (Giroto et al., 2015; Xiong et al., 2018) and Brushite (Hermassi et al., 2017) have been investigated as potential slow release fertilisers, HAP and brushite nanoparticle embedded inside a Ca_2Al matrix may offer promising PO4 slow release properties.

5. Acknowledgements

This work was partially funded by the The Innovation Fund Denmark via the project "RecoverP". UGN, LL, and NDJ acknowledges financial support from the Villum Foundation via the "Villum Young Investigator Programme" (grant VKR022364) and the 600 MHz

NMR (Villum Center for Bioanalytical Services). The authors thanks Joel Cellier, assistant-engineer at ICCF for the conception of the in-situ XRD cell.

6. References

Andersen M.D., Jakobsen H.J., Skibsted J., 2002. Characterization of the α–β Phase Transition in Friedels Salt ($Ca_2Al(OH)_6Cl{\cdot}2H_2O$) by Variable-Temperature 27Al MAS NMR Spectroscopy. J. Phys. Chem. A. 106 (28), 6676-6682.

Aue W.P., Roufosse A.H., Glimcher, M.J.; Griffin, R.G., 1984. Solid-state Phosphorus-3 1 Nuclear Magnetic Resonance Studies of Synthetic Solid Phases of Calcium Phosphate: Potential Models of Bone Mineral. Biochemistry 23, 6110-6114.

Bell L.C., H. Mika, Kruger B.J., 1978. Synthetic hydroxyapatite-solubility product and stoichiometry of dissolution. Archs Oral Biol. 23, 329-336.

Bernardo M.P., Moreira F.K.V., Ribeiro C., 2017 Synthesis and characterization of eco-friendly Ca-Al-LDH loaded with phosphate for agricultural applications. Applied Clay Science. 137, 143-150.

Broberg O., Pettersson K., 1988. Analytical determination of orthophosphate in water. Hydrobiologia 170 (1), 45-59.

Chen X., 2015. Modeling of Experimental Adsorption Isotherm Data. Information, 6 (1), 14-22.

Chen X., Kong H., Wu D., Wang X., Lin Y., 2009. Phosphate removal and recovery through crystallization of hydroxyapatite using xonotlite as seed crystal. J. Environ. Sci. 21 (5), 575-580.

Cieślik B., Konieczka P., 2017. A review of phosphorus recovery methods at various steps of wastewater treatment and sewage sludge management. The concept of “no solid waste generation” and analytical methods. J. Clean. Prod. 142, 1728-4170.

DEaI EC, 2013. CRM for the EU Report of the ad hoc working group on defining critical raw materials. Report 1-84.

Desmidt E., Ghyselbrecht K., Zhang Y., Pinoy L., Van der Bruggen B., Verstraete W, Rabaey K., Meesschaert B., 2015. Global Phosphorus Scarcity and Full-Scale P-Recovery Techniques: A Review. Crit. Rev. Env. Sci. Technol. 45 (4), 336-384.

Di Bitetto A.E., Carteret C., Durand P., Kervern G., 2017. Probing the Dynamics of Layered Double Hydroxides by Solid-State 27Al NMR Spectroscopy. J. Phys. Chem. C. 121 (13), 7276-7281.

Everaert M., Warrinnier ., Baken S., Gustafsson J.P., De Vos D., Smolders E., 2016. Phosphate-Exchanged Mg–Al Layered Double Hydroxides: A New Slow Release Phosphate Fertilizer. ACS Sustainable Chem. Eng., 4 (8), 4280–4287.

Everaert M., Slenders K., Dox K., Smolders S., De Vos D., Smolders E., 2018. The isotopic exchangeability of phosphate in Mg-Al layered double hydroxides. J. Colloid Interface Sci. 520, 25-32.

Farley M., 2012. Eutrophication in Fresh Waters: An International Review. In: Bengtsson L, Herschy RW, Fairbridge RW, editors. Encyclopedia of Lakes and Reservoirs. Dordrecht: Springer Netherlands, 258-270.

Fowler B.O., Kuroda S., 1986. Changes in heated and in laser-irradiated human tooth enamel and their probable effects on solubility. Calcif Tissue Int. 38, 197-208.

François M., Renaudin G., Evrard O., 1998. A Cementitious Compound with Composition 3CaO- Al_2O_3-$CaCO_3$-11H_2O. Acta Cryst. Sec C. C54, 1214-1217.

Gacsi A., Kutus B., Kónya Z., Kukovecz Á., Pálinkó I., Sipos P., 2016. Estimation of the solubility product of hydrocalumite–hydroxide, a layered double hydroxide with the formula of $[Ca_2Al(OH)_6]OH \cdot nH_2O$. J. Phys. Chem. Solids 98, 167–173.

Gibson I.R., Bonfield W., 2002. Novel synthesis and characterization of an AB-type carbonate-substituted hydroxyapatite. J. Biomed. Mater. Res. 59 (4), 697-708.

Giles C.H., Smith D., Huitson A., 1974 A general treatment and classification of the solute adsorption isotherm. I. Theoretical. J. Colloid Interface Sci. 47 (3), 755-765.

Giroto A.S., Fidelis S.C., Ribeiro C., 2015. Controlled release from hydroxyapatite nanoparticles incorporated into biodegradable, soluble host matrixes. RSC Advances 5, 104179-104186.

Gregory T.M., Moreno E.C., Moreno W.E., 1970. Solubility of $CaHPO_4.2H_2O$ in the system $Ca(OH)_2$-H_3PO_4-H_2O at 5, 15, 25 and 37.5°C. J. Res. Natl. Bur. Stand. 74, 461-475.

Hatami H., Fotovat A., Halajnia A., 2018. Comparison of adsorption and desorption of phosphate on synthesized Zn-Al LDH by two methods in a simulated soil solution. Applied Clay Science 152, 333-341.

Hermassi M., Valderrama C., Moreno N., Font O., Querol X., Batis N. H., Cortina J. L., 2017. Fly ash as reactive sorbent for phosphate removal from treated waste water as a potential slow release fertilizer. Journal of Environmental Chemical Engineering 5, 160-169.

Jensen N.D., Bjerring M., Nielsen U.G., 2016. A solid state NMR study of layered double hydroxides intercalated with para-amino salicylate, a tuberculosis drug. Solid State Nucl. Magn. Reson. 78, 9-15.

Jia Y., Wang H., Zhao X., Liu X., Wang Y., Fan Q., Zhou J., 2016. Kinetics, isotherms and multiple mechanisms of the removal for phosphate by Cl-hydrocalumite. Applied Clay Science 129, 116-121.

Jeong-Woo Son, Jae-Hyun Kim, Jin-Kyu Kang, Song-Bae Kim, Jeong-Ann Park, Chang-Gu Lee, Jae-Woo Choi & Sang-Hyup Lee, 2016. Analysis of phosphate removal from aqueous solutions by hydrocalumite. Desalination and Water Treatment 57(45), 21476-21486.

Kemp T., Smith M., 2009. QuadFit--a new cross-platform computer program for simulation of NMR line shapes from solids with distributions of interaction parameters. Solid State Nucl. Magn. Reson. 35 (4), 243-252.

Khitous M., Salem Z., Halliche D., 2016. Removal of phosphate from industrial wastewater using uncalcined MgAl-NO_3 layered double hydroxide: batch study and modeling. Desalin. Water Treat. 57 (34), 15920-15931.

Lazaridis N.K., 2003. Sorption Removal of Anions and Cations in Single Batch Systems by Uncalcined and Calcined Mg-Al-CO_3 Hydrotalcite. Water, Air, Soil Pollut. 146 (1-4), 127-139.

Lu Y., Hou H., Zhao J., Zhou J., Liu J., Feng L., Quian G., Xu Y., 2016. Enhanced removal of phosphate by hydrocalumite: synergism of AlPO4 and CaHPO4·2H2O precipitation. Desalin.Water Treat. 57 (17), 7841-7846.

Lu Y., Zhao J., Zhou, J., Liu J., Feng L., Qian G., Xu Y., 2015. Enhanced removal of phosphate by hydrocalumite: synergism of AlPO4 and CaHPO4·2H2O precipitation. Desalin.Water Treat. 1-6.

Oliveira M., Machado A.V., 2013. The role of phosphorus on eutrophication: a historical review and future perspectives. Environ. Technol. Rev. 2(1), 117-127.

Pushparaj S.S.C., Forano C., Prevot V., Lipton A.S., Rees G.J., Hanna J..V, Nielsen U.G., 2015. How the Method of Synthesis Governs the Local and Global Structure of Zinc Aluminum Layered Double Hydroxides. J. Phys. Chem. C. 119 (49), 27695-27707.

Qian G, Feng L, Zhou JZ, Xu Y, Liu J, Zhang J, Xu Z.P., 2012. Solubility product (Ksp)-controlled removal of chromate and phosphate by hydrocalumite. Chem. Eng. J. 181-182, 251-258.

Onac B.P., Sumrall J., Mylroie J.E., Kearns J., 2009. Cave Minerals of San Salvador Island, Bahamas. Environmental Sustainability Books, Ed. University of South Florida Tampa Library, Tampa, 2009.

Qiu X., Sasaki K., Takaki Y., Hirajima T., Ideta K., Miyawaki J., 2015. Mechanism of boron uptake by hydrocalumite calcined at different temperatures. J. Hazard. Mater. 287, 268-277.

Radha A.V., Vishnu K.P., Shivakumara C., 2005. Mechanism of the anion exchange reactions of the layered double hydroxides (LDH) of Ca and Mg with Al. Solid State Sciences 7 (10), 1180-1187.

Renaudin G., François M., 1999. The lamellar double-hydroxide (LDH) compound with composition $3CaO.Al_2O_3.Ca(NO_3)_2.10H_2O$. Acta Crystallogr., Sect. C: Cryst. Struct. Commun. 55, 835-838.

Renaudin G., Francois M., Evrard O., 1999. Order and disorder in the lamellar hydrated tetracalcium monocarboaluminate compound. Cement and Concrete Research. 29 (1), 63-69.

Ricardo R., 2012. Layered double hydroxides applications as sorbents for environmental remediation. In Hydroxides: Synthesis, types and applications. Editors: Carillo A.C., Griego D.A., Chapt. 2, Publisher: Nova Science Pub, Ic., 39-71.

Rothwell W. P., Waugh J.S., Yesinowski J.P., 1980. High-resolution variable-temperature phosphorus-31 NMR of solid calcium phosphates. J. Am. Chem. Soc. 1102 (8), 2637–2643.

Schröder JJ, Smit AL, Rosemarin A., 2009. Use of Phosphorus. EU Tender ENVB1/ETU/2009/0025, SEI Report, 1-140.

Sideris P.J., Blanc F., Gan Z., Grey C.P., 2012. Identification of Cation Clustering in Mg–Al Layered Double Hydroxides Using Multinuclear Solid State Nuclear Magnetic Resonance Spectroscopy. Chem. Mater. 24 (13), 2449-2461.

Sideris P.J., Nielsen U.G., Gan Z., Grey C.P., 2008. Mg/Al Ordering in Layered Double Hydroxides Revealed by Multinuclear NMR Spectroscopy. Science 321 (5885), 113-7.

Seftel E.M., Ciocarlan R.G., Michielsena B., Meynena V., Mullensa S., Cool P., 2018. Insights into phosphate adsorption behavior on structurally modified ZnAl layered double hydroxides. Applied Clay Science 165, 234–246.

Swamiappan S., 2016. Synthesis of carbonate substituted hydroxyapatite by Pechini method. Kuwait J. Sci. 43, 174-184.

Talboys P.J., Heppell J., Roose T., Healey J.R., Jones D.L., Withers P.J.A., 2016. Struvite: a slow-release fertiliser for sustainable phosphorus management? Plant Soil 401 (1-2), 109-123.

Tsuji H., Fujii S., 2014. Phosphate recovery by generating hydroxyapatite via reaction of calcium eluted from layered double hydroxides. Applied Clay Science 99, 261-265.

Tung M.S., Eidelman N., Sieck B., Brown W.E., 1988. Octacalcium phosphate solubility product from 4 to 37C. J. Res. Natl. Bur. Stand. 93, 613-624.

Vieille L., Rousselot I., Leroux F., Besse J.P., Taviot-Guého C., 2003. Hydrocalumite and Its Polymer Derivatives. 1. Reversible Thermal Behavior of Friedel's Salt: A Direct

Observation by Means of High-Temperature in Situ Powder X-ray Diffraction. Chem. Mater. 15 (23), 4361-4368.

Wan S., Wang S., Li Y., Gao B., 2017. Functionalizing biochar with Mg–Al and Mg–Fe layered double hydroxides for removal of phosphate from aqueous solutions. J. Ind. Eng. Chem. 47, 246-253.

Xiong Lei, Wang Peng, Kopittke Peter M., 2018. Tailoring hydroxyapatite nanoparticles to increase their efficiency as phosphorus fertilisers in soils. Geoderma 323, 116-125.

Xu Y., Dai Y., Zhou J., Xu Z.P., Qian G., Lu G.Q.M., 2010. Removal efficiency of arsenate and phosphate from aqueous solution using layered double hydroxide materials: intercalation vs. precipitation. J. Mater. Chem. 20 (22), 4684-4691.

Ye Z., Shen Y., Ye X., Zhang Z., Chen S., Shi J., 2014. Phosphorus recovery from wastewater by struvite crystallization: Property of aggregates. J. Environ. Sci. 26 (5), 991-1000.

Zhang P., Qian G., Cheng H., Yang J., Shi H., Frost R.L., 2011. Near-infrared and mid-infrared investigations of Na-dodecylbenzenesulfate intercalated into hydrocalumite chloride (CaAl-LDH-Cl). Spectrochim. Acta, Part A 79 (3), 548-553.

Zhou J., Yang S., Yu J., Shu Z., 2011. Novel hollow microspheres of hierarchical zinc-aluminum layered double hydroxides and their enhanced adsorption capacity for phosphate in water. J. Hazard. Mater. 192 (3), 1114-1121.

Zhou J.Z., Feng L., Zhao J., Liu J., Liu Q., Zhang J., Quian G., 2012. Efficient and controllable phosphate removal on hydrocalumite by multi-step treatment based on pH-dependent precipitation. Chem. Eng. J. 185-186, 219-225.

Tables and Figures

Figure legends

Fig. 1: (A) XRD pattern and (B) FTIR spectrum of $Ca_2Al\text{-}NO_3$.

Fig. 2: A) Experimental and calculated adsorption isotherms of $Ca_2Al\text{-}NO_3/HPO_4^{2-}$ system. B) Insert linear form of the Langmuir fit.

Fig.3: A) ex-situ XRD of $Ca_2Al\text{-}NO_3/HPO_4^{2-}$ series for various HPO_4^{2-} loading at 0; 0.3; 0.4; 0.5; 0.6; 0.7; 0.8; 0.9 g/L (⩛ $Ca_2Al\text{-}NO_3$; ✦ $Ca_2Al\text{-}CO_3$; ✧ $Al(OH)_3$ Gibbsite; ♦ $Ca_5(PO_4)_3(OH)$ Hydroxyapatite; ✸$Ca(HPO_4).2H_2O$ Brushite) and B) in-situ XRD of $Ca_2Al\text{-}NO_3$ in contact with a 2M HPO_4^{2-} solution.

Fig. 4: Raman spectra of the $Ca_2Al\text{-}NO_3/HPO_4^{2-}$ series with increasing HPO_4^{2-} loading (from 0.3 to 0.9 g/L) at A) medium and B) low energy range.

Figure 5: The ^{27}Al MAS NMR spectra of the LDH exposed to the different phosphate concentrations. The dotted line shows the position of resonance for $Ca_2Al\text{-}NO_3$ LDH.

Fig. 6: Deconvolutions of the ^{31}P MAS NMR spectra of the $Ca_2Al\text{-}NO_3$ LDH with different phosphate loadings a-g): $Ca_2Al\text{-}NO_3$ with 0.3-0.P, h): hydroxyapatite and j) brushite, two resonances from impurities are observed at 0.1 and -1.4 ppm. The top line is the experimental spectrum (Exp), the second is the simulated (Sim) and the bottom line is the residual (Dif).

Fig. 7: SEM images of A) pristine $Ca_2Al\text{-}NO_3$ material and loaded with various amounts of PO_4, B) Ca0.3P, C) Ca0.6P, D) Ca0.9P.

Fig. 8: Initial step of the conversion of $Ca_2Al\text{-}NO_3$ LDH into calcium phosphate minerals.

Fig. 2

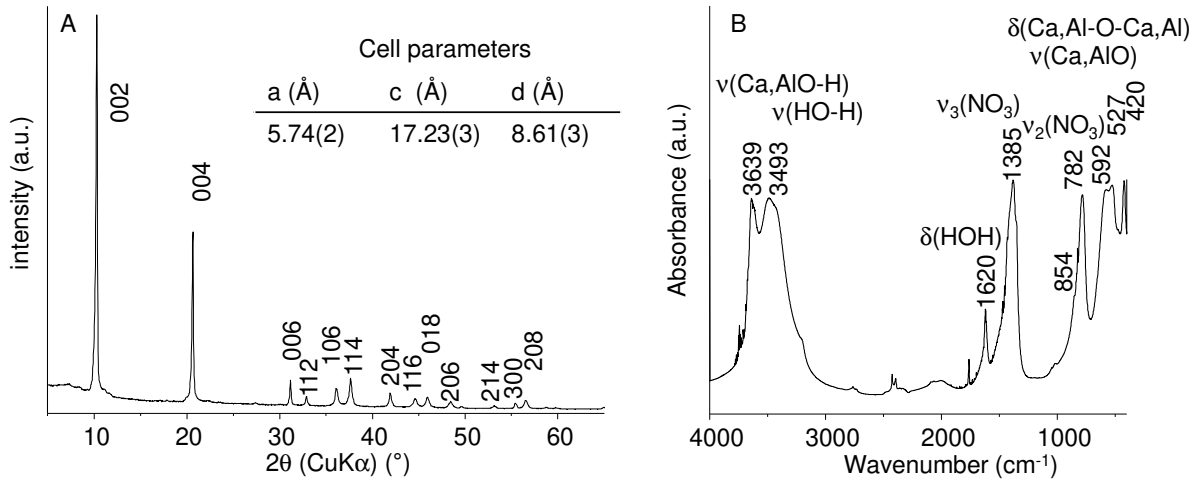
A
Cell parameters
a (Å) c (Å) d (Å)
5.74(2) 17.23(3) 8.61(3)
intensity (a.u.)
002
004
006
112
106
114
204
116
018
206
214
300
208
2θ (CuKα) (°)
B
δ(Ca,Al-O-Ca,Al)
ν(Ca,AlO)
ν(Ca,AlO-H)
ν(HO-H)
ν3(NO3)
ν2(NO3)
3639
3493
1385
527
420
782
592
δ(HOH)
1620
854
Absorbance (a.u.)
Wavenumber (cm-1)

Fig. 2

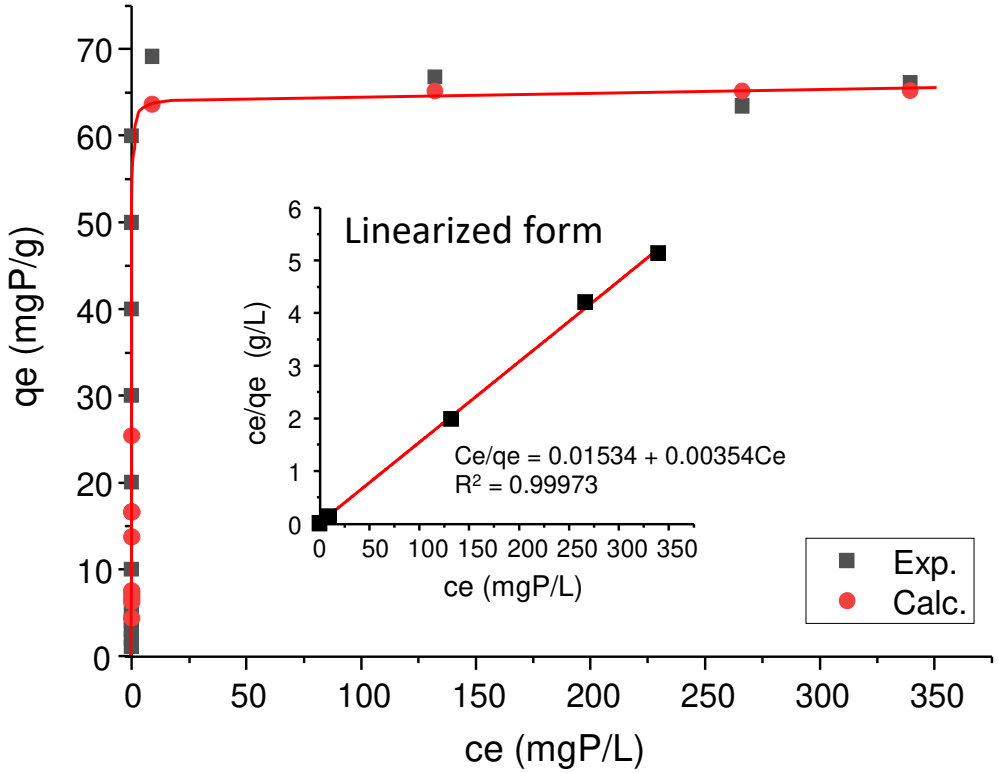
qe (mgP/g)
ce (mgP/L)
Linearized form
ce/qe (g/L)
Ce/qe = 0.01534 + 0.00354Ce
R² = 0.99973
ce (mgP/L)
Exp.
Calc.

Fig. 3

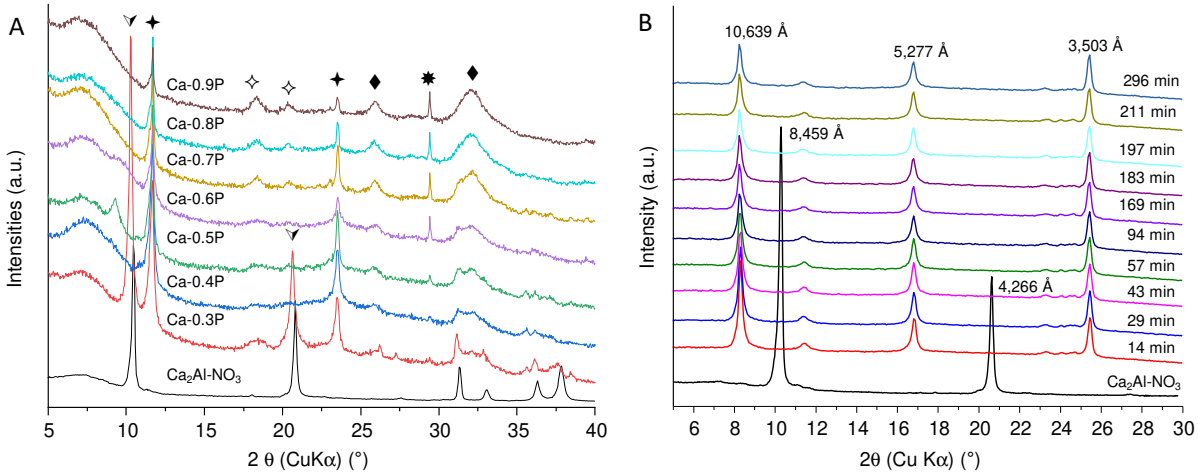
A
Intensities (a.u.)
Ca-0.9P
Ca-0.8P
Ca-0.7P
Ca-0.6P
Ca-0.5P
Ca-0.4P
Ca-0.3P
Ca2Al-NO3
2 θ (CuKα) (°)
B
Intensity (a.u.)
10,639 Å
5,277 Å
3,503 Å
8,459 Å
4,266 Å
296 min
211 min
197 min
183 min
169 min
94 min
57 min
43 min
29 min
14 min
Ca2Al-NO3
2θ (Cu Kα) (°)

Fig. 4

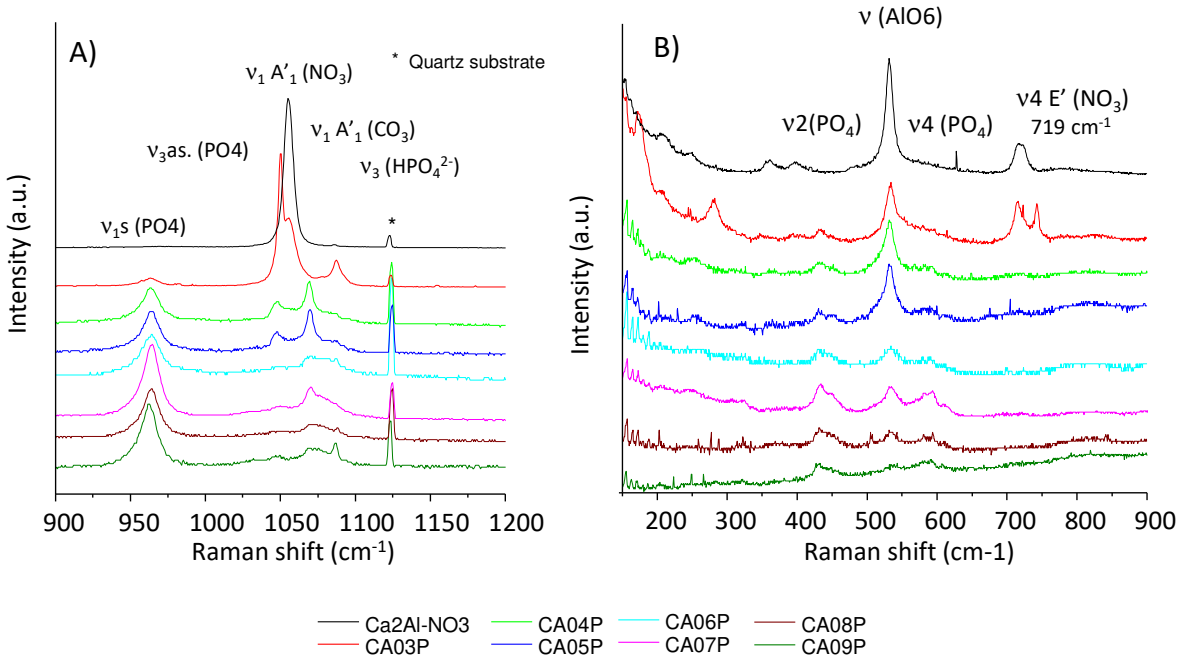
A)
Intensity (a.u.)
ν1 A'1 (NO3)
* Quartz substrate
ν1 A'1 (CO3)
ν3as. (PO4)
ν3 (HPO4 2-)
ν1s (PO4)
Raman shift (cm-1)
B)
ν (AlO6)
ν2(PO4)
ν4 (PO4)
ν4 E' (NO3)
719 cm-1
Intensity (a.u.)
Raman shift (cm-1)
Ca2Al-NO3
CA03P
CA04P
CA05P
CA06P
CA07P
CA08P
CA09P

Fig. 5

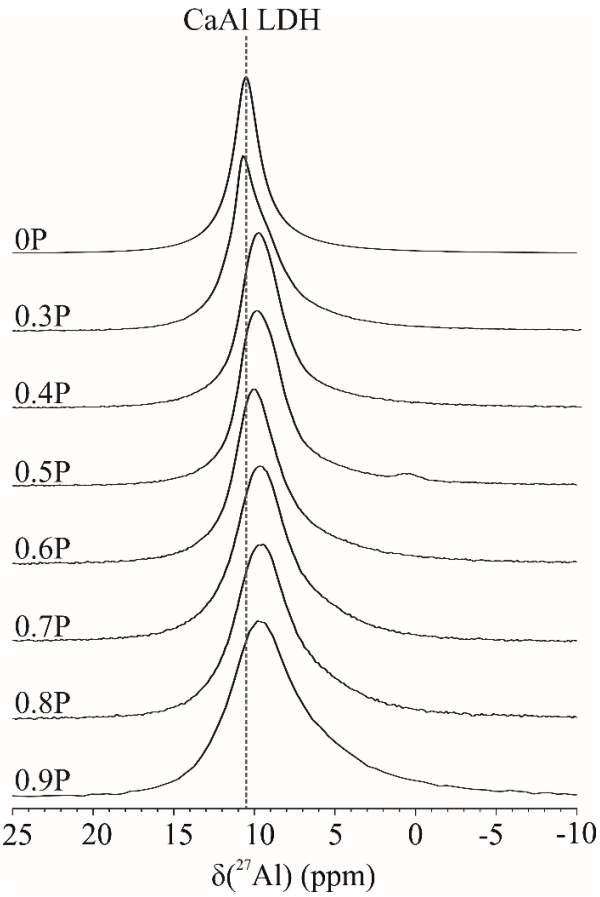
CaAl LDH
0P
0.3P
0.4P
0.5P
0.6P
0.7P
0.8P
0.9P
25
20
15
10
5
0
-5
-10
δ(27Al) (ppm)

Fig. 6

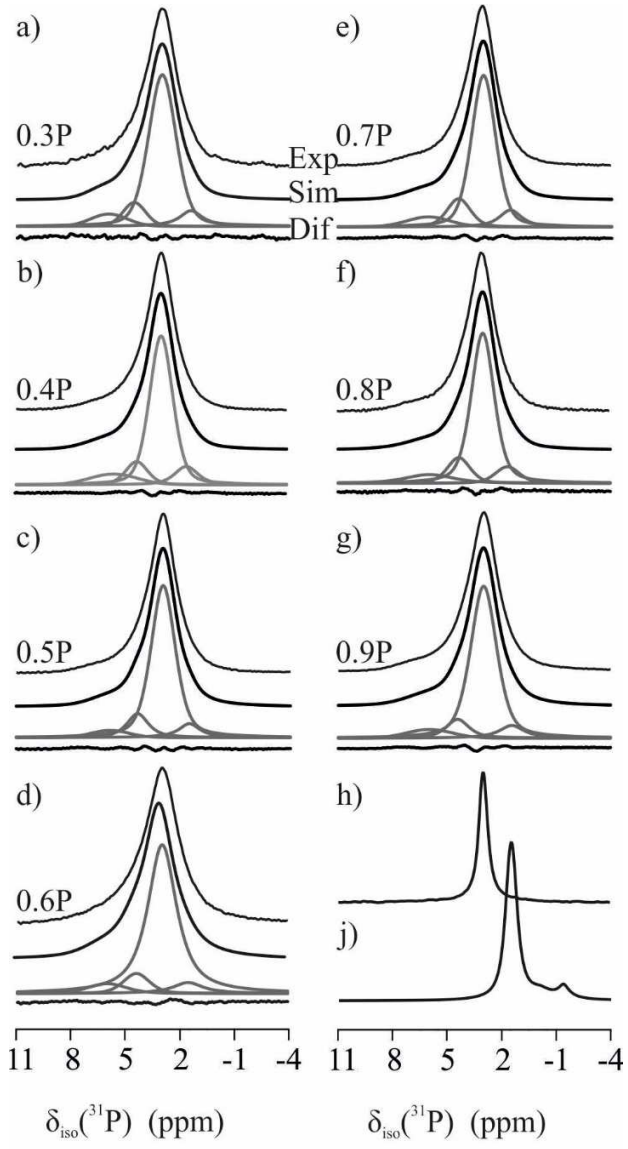
a)
0.3P
Exp
Sim
Dif
b)
0.4P
c)
0.5P
d)
0.6P
e)
0.7P
f)
0.8P
g)
0.9P
h)
j)
11 8 5 2 -1 -4
11 8 5 2 -1 -4
δiso(31P) (ppm)
δiso(31P) (ppm)

Fig. 7

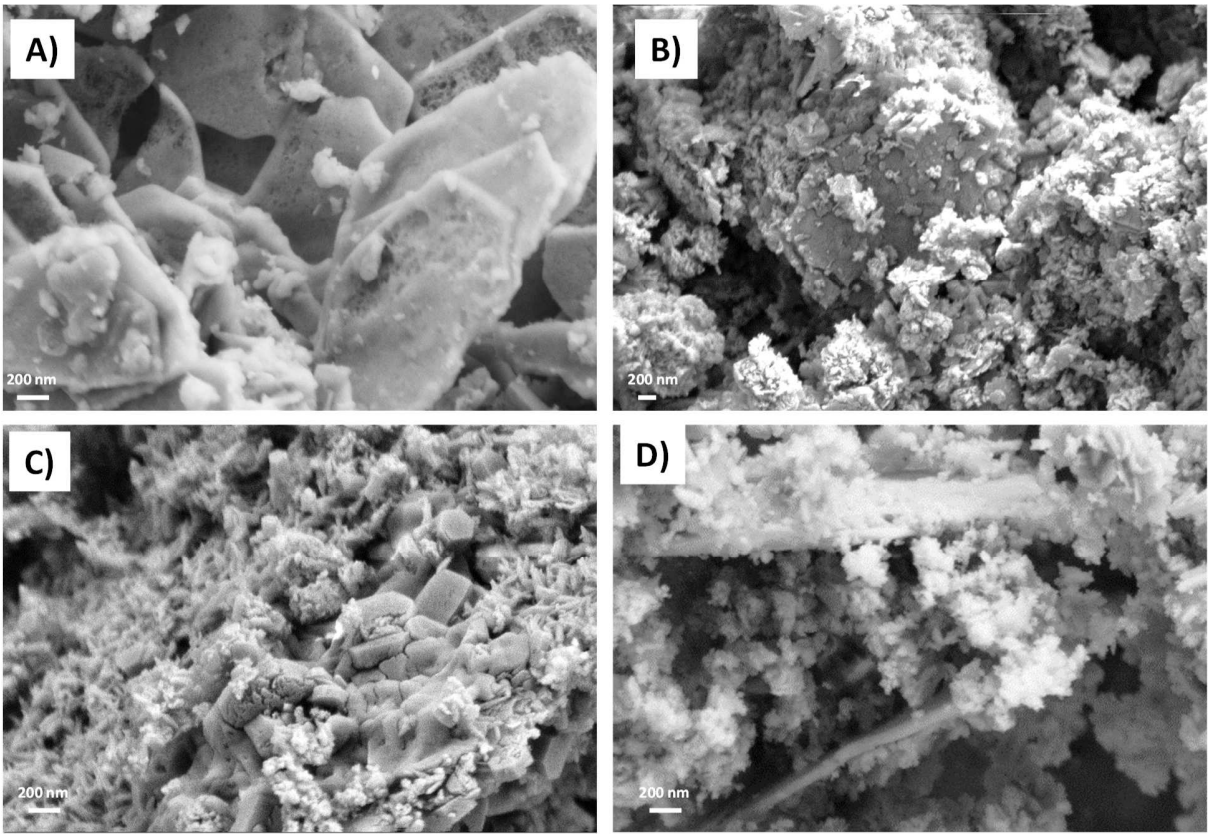
A)
200 nm
B)
200 nm
C)
200 nm
D)
200 nm

Fig. 8

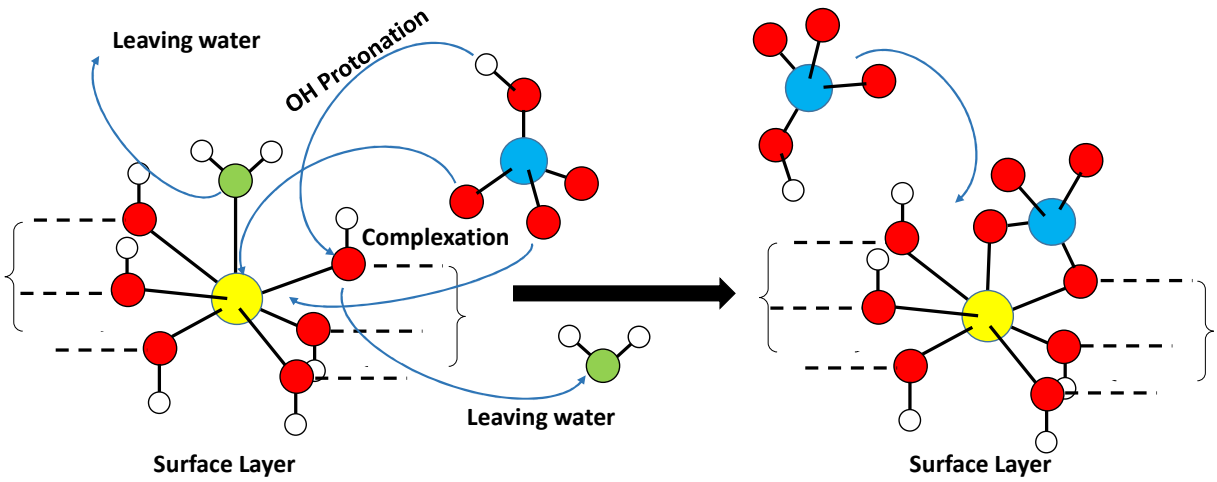
Leaving water
OH Protonation
Complexation
Leaving water
Surface Layer
Surface Layer

Tables and Figures

Table legends

Table 1: Solubility products of some calcium phosphate compounds.

Table 2: Assignment of PO_4 infrared and Raman vibration bands.

Table 3: Parameters obtained from the deconvolutions of the ^{31}P MAS NMR spectra for Ca_2Al-NO_3.

Table 1

Calcium phosphate phases	pKsp	Ref.
$Ca_5(PO)_4(OH)$	-58.4	(Bell et al., 1978)
$Ca_3(PO_4)_2$	-25.5	(Fowler et al., 1986)
$Ca_8H_2(PO_4)_6.5H_2O$	-96.6	(Tung et al., 1988)
$CaHPO_4.2H_2O$	-6.59	(Gregory et al., 1970)
$Ca_2Al(OH)_6(OH).2H_2O$	-11.4	(Gacsi et al., 2016)

Table 2

Vibrations (cm^{-1})	Infrared	Raman
ν_3 $(PO_4)_{as}$	1025, 1063, 1105, 1138	1070; 1081
ν_1 $(PO_4)_s$		962; 1050

Table 3:

Sample	Assignment	$\delta_{iso}(^{31}P)$(ppm)	I(%)
	Brushite	1.4(5)	8(5)
	Hydroxyapatite	3.0(3)	75(6)
		4.5(6)	10(5)
$Ca_2Al\text{-}NO_3$ 0.3P	Oxyhydroxyapatite phase	6.0(7)	8(5)
	Brushite	1.6(5)	9(5)
	Hydroxyapatite	3.0(3)	71(6)
		4.3(6)	10(5)
$Ca_2Al\text{-}NO_3$ 0.4P	Oxyhydroxyapatite phase	5.6(7)	10(5)
	Brushite	1.5(5)	7(6)
	Hydroxyapatite	3.0(3)	77(8)
		4.3(6)	11(6)
$Ca_2Al\text{-}NO_3$ 0.5P	Oxyhydroxyapatite phase	5.9(7)	5(6)
	Brushite	1.5(5)	6(5)
	Hydroxyapatite	3.0(3)	79(6)
		4.4(6)	9(5)
$Ca_2Al\text{-}NO_3$ 0.6P	Oxyhydroxyapatite phase	6.0(7)	6(5)
	Brushite	1.5(5)	8(5)
	Hydroxyapatite	3.0(3)	71(6)
		4.4(6)	13(5)
$Ca_2Al\text{-}NO_3$ 0.7P	Oxyhydroxyapatite phase	6.0(7)	8(5)
	Brushite	1.7(5)	8(5)
	Hydroxyapatite	3.0(3)	71(6)
		4.4(6)	12(5)
$Ca_2Al\text{-}NO_3$ 0.8P	Oxyhydroxyapatite phase	6.0(7)	9(5)
	Brushite	1.4(5)	7(5)
	Hydroxyapatite	3.0(3)	77(6)
		4.4(6)	9(5)
$Ca_2Al\text{-}NO_3$ 0.9P	Oxyhydroxyapatite phase	6.0(7)	7(6)

The dominating resonance at $\delta_{iso}(^{31}P)$ = 3.0(3) ppm constitutes 71-79 % of the phosphates species and is based on the isotropic shift assigned to hydroxyapatite

Graphical abstract